Supplementary Information

Porosity and Structure of Hierarchically Porous Ni/Al_2O_3 Catalysts for CO_2 Methanation

Sebastian Weber [1,2], Ken L. Abel [3], Ronny T. Zimmermann [4], Xiaohui Huang [5,6], Jens Bremer [7], Liisa K. Rihko-Struckmann [7], Darren Batey [8], Silvia Cipiccia [8], Juliane Titus [3], David Poppitz [3], Christian Kübel [5,6,9], Kai Sundmacher [4,7], Roger Gläser [3] and Thomas L. Sheppard [1,2,*]

[1] Institute of Catalysis Research and Technology, Karlsruhe Institute of Technology (KIT), Hermann-von-Helmholtz-Platz 1, 76344 Eggenstein-Leopoldshafen; sebastian.weber@kit.edu, thomas.sheppard@kit.edu

[2] Institute for Chemical Technology and Polymer Chemistry, Karlsruhe Institute of Technology (KIT), Engesserstraße 20, 76131 Karlsruhe, Germany; sebastian.weber@kit.edu, thomas.sheppard@kit.edu

[3] Institute of Chemical Technology, Universität Leipzig, Linnéstr. 3, 04103 Leipzig, Germany; ken.abel@uni-leipzig.de, juliane.titus@uni-leipzig.de, david.poppitz@uni-leipzig.de, roger.glaeser@uni-leipzig.de

[4] Otto von Guericke University Magdeburg, Chair for Process Systems Engineering, Universitätplatz 2, 39106 Magdeburg; ronny.zimmermann@mpi-magdeburg.mpg.de, sundmacher@mpi-magdeburg.mpg.de

[5] Institute of Nanotechnology (INT), Karlsruhe Institute of Technology (KIT), Hermann-von-Helmholtz-Platz 1, 76344, Eggenstein-Leopoldshafen, Germany; xiaohui.huang@partner.kit.edu, christian.kuebel@kit.edu

[6] Department of Materials and Earth Sciences, Technische Universität Darmstadt, Alarich-Weiss-Straße 2, 64287 Darmstadt, Germany; christian.kuebel@kit.edu

[7] Max Planck Institute Magdeburg, Department Process Systems Engineering, Sandtorstraße 1, 39106 Magdeburg; bremerj@mpi-magdeburg.mpg.de, rihko@mpi-magdeburg.mpg.de, sundmacher@mpi-magdeburg.mpg.de

[8] Diamond Light Source, Harwell Science and Innovation Campus, Fermi Ave, Didcot OX11 0DE, UK; darren.batey@diamond.ac.uk, silvia.cipiccia@diamond.ac.uk

[9] Karlsruhe Nano Micro Facility, Karlsruhe Institute of Technology (KIT), Hermann-von-Helmholtz-Platz 1, 76344 Eggenstein-Leopoldshafen, Germany; christian.kuebel@kit.edu

* Correspondence: thomas.sheppard@kit.edu; Tel.: +49 721 608 47989

Content

1. Results Rietveld Refinement

The structural parameters as obtained from Rietveld refinement using initial structural models by Zhou *et al.*[1] for Al_2O_3 and O'Neill *et al.*[2] for $NiAl_2O_4$ are listed in Table S1. Two cases were studied, first with refined Al occupancies and second with fixed Al occupancies according to the literature data.

Table S1 Structural parameters obtained from Rietveld analysis for the refinements of Ni/Al_2O_3-h with refined and fixed occupancies of the Al positions of the Al_2O_3 phase.

	Refined Al occupancies				**Fixed Al occupancies**			
R_{exp}	2.49				2.49			
R_{wp}	2.05				4.87			
GoF	0.82				1.96			
Phase	Al_2O_3		$NiAl_2O_4$		Al_2O_3		$NiAl_2O_4$	
Space group	$Fd\bar{3}mZ$		$Fd\bar{3}m$:2		$Fd\bar{3}mZ$		$Fd\bar{3}m$:2	
Phase amount / wt.%	95.50(13)		4.50(13)		84.29(12)		15.71(12)	
Crystallite size *D* / nm	6.933(19)		7.41(13)		7.03(7)		6.77(6)	
a / Å	8.0133(2)		8.0604(11)		8.0080(6)		8.0305(9)	
Phase	Al_2O_3				Al_2O_3			
Atom	*x*	*y*	*z*	*occ*	*x*	*y*	*z*	*occ*
O1	0.25470	0.25470	0.25470	1	0.25470	0.25470	0.25470	1
Al1	½	½	½	1.156(7)	½	½	½	0.58
Al2	⅛	⅛	⅛	0.839(4)	⅛	⅛	⅛	0.84
Al3	0.02720	0.02720	0.02720	0.0133(13)	0.02720	0.02720	0.02720	0.17
Phase	$NiAl_2O_4$				$NiAl_2O_4$			
Atom	*x*	*y*	*z*	*occ*	*x*	*y*	*z*	*occ*
O	0.25490	0.25490	0.25490	1	0.25490	0.25490	0.25490	1
Al1	½	½	½	1	½	½	½	1
Al2	⅛	⅛	⅛	1	⅛	⅛	⅛	1
Ni1	½	½	½	1	½	½	½	1
Ni2	⅛	⅛	⅛	1	⅛	⅛	⅛	1

2. Tomography Studies

2.1. Resolution Estimation ET

To estimate the resolution of the ET in terms of sharpness, we performed a line profile analysis of an edge feature of the SIRT reconstructed tomograms. We analyzed the 10-90% rise distance of the edge as shown in Figure S1 and Figure S2.

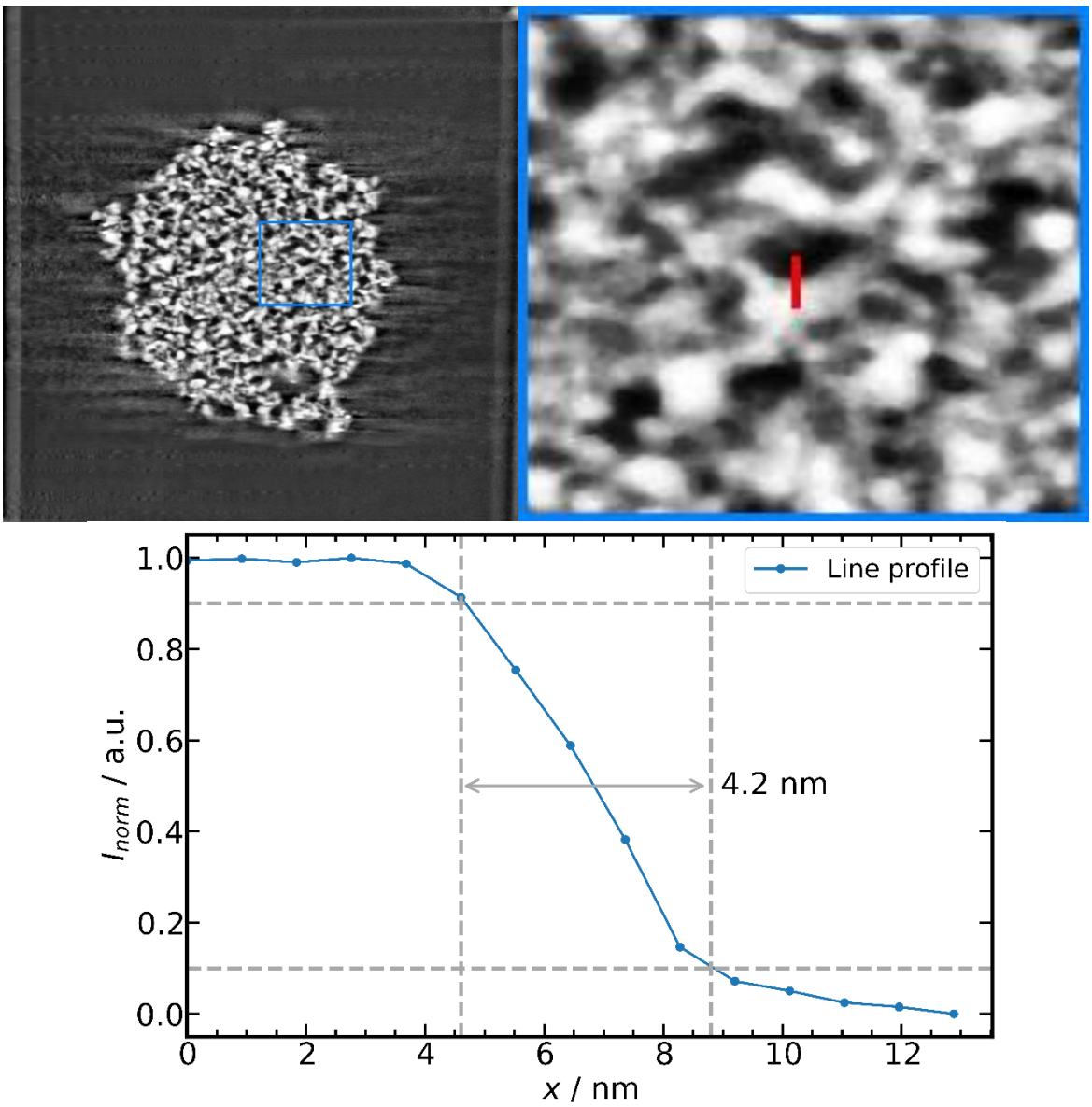

Figure S1 Selected slice of the SIRT reconstructed ET1. The blue box depicts the area shown zoomed for the line profile (red) analysis to estimate the resolution of the tomogram. The estimated resolution by the 10%-90% criteria for the selected line profile is 4.2 nm.

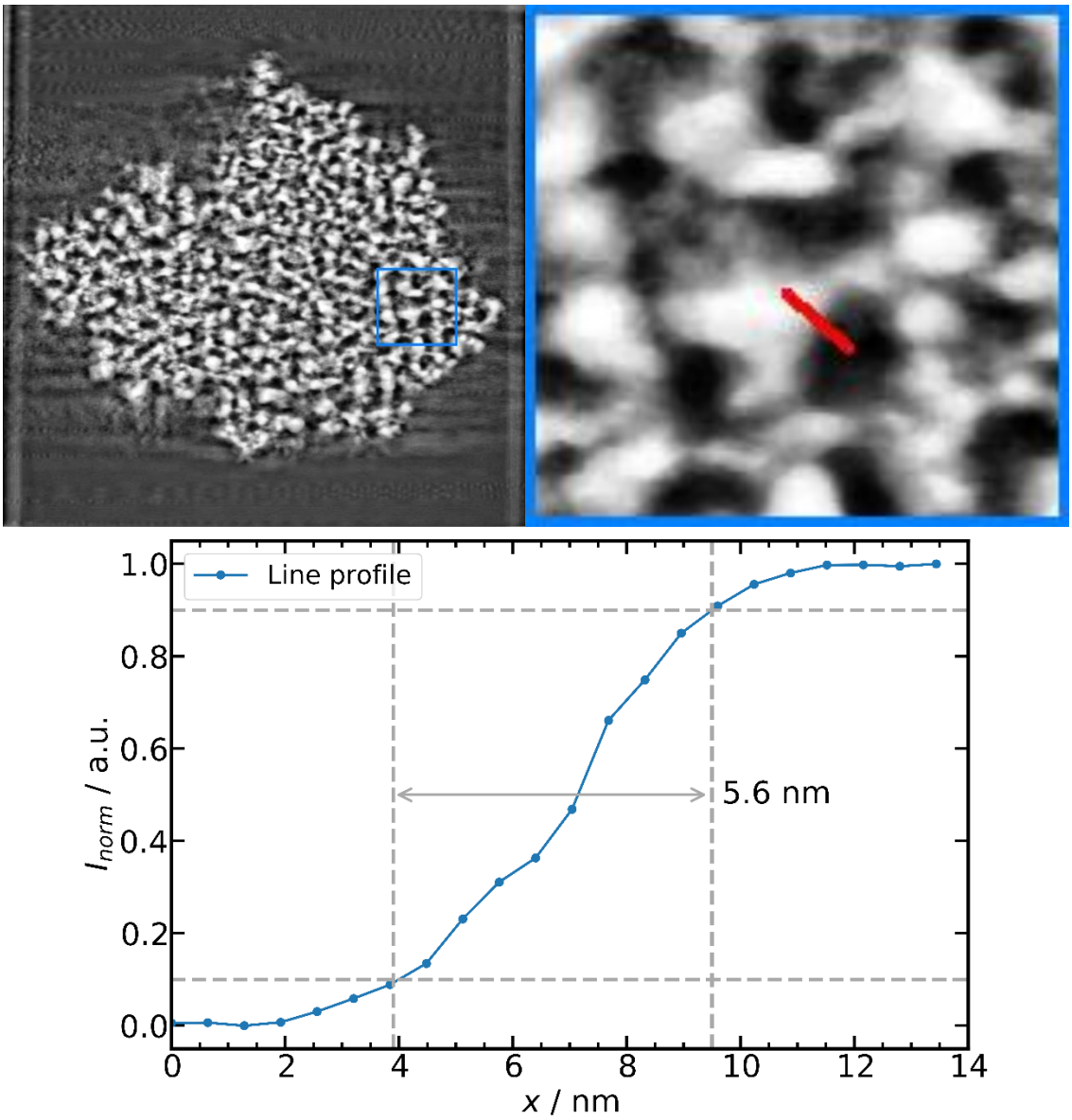

Figure S2 Selected slice of the SIRT reconstructed ET2. The blue box depicts the area shown zoomed for the line profile (red) analysis to estimate the resolution of the tomogram. The estimated resolution by the 10%-90% criteria for the selected line profile is 5.6 nm.

2.2. Sample preparation PXCT

The Ni/Al_2O_3-h sample for the PXCT experiment, mounted on an Al-pin of the OMNY design [3], is shown in Figure S3. The sample was mounted in a FEI Strata 400 S FIB/SEM by transferring the respective particle with a micro-manipulator and Pt-gluing to the tip of the pin.

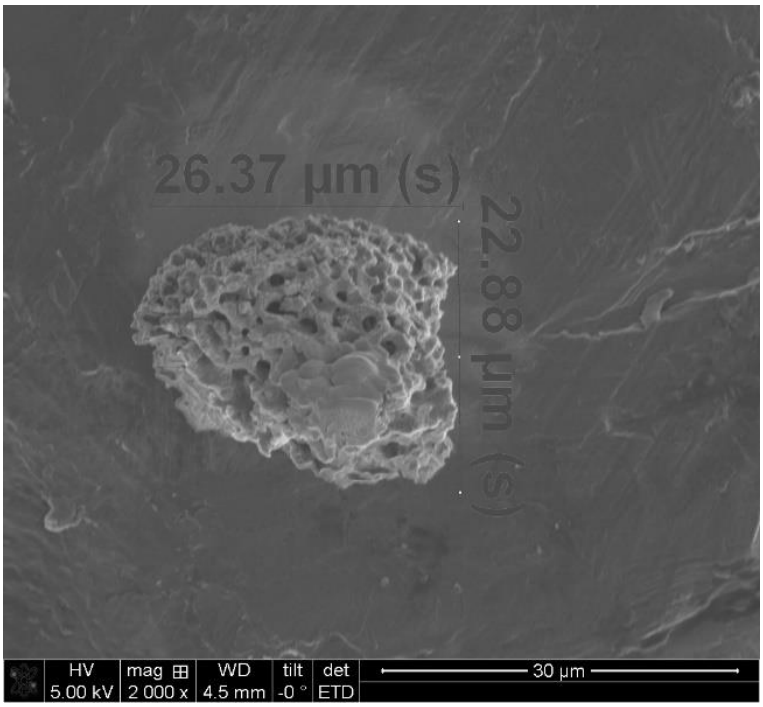

Figure S3 SEM images of the Ni/Al_2O_3-h sample mounted on the Al-pin for the PXCT experiment with dimensions measured in the SEM.

2.3. PXCT uncropped tomogram

The PXCT of the Ni/Al_2O_3-h sample was cropped before performing the image analysis to remove the big Pt residue from the sample transfer. The original volume of the PXCT and the cropped one are shown in Figure S4.

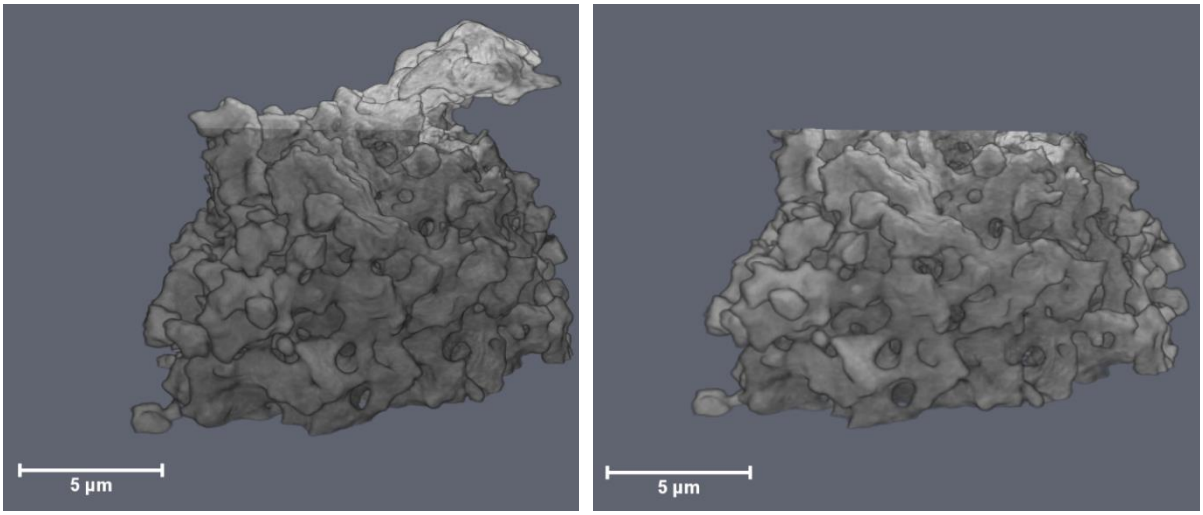

Figure S4 Uncropped PXCT of the Ni/Al_2O_3-h sample (left) and cropped tomogram (right). The cropped feature on top mostly consists of Pt as residue of the sample preparation with the micromanipulator within the FIB.

2.4. Resolution Estimation PXCT

The resolution of the PXCT of the Ni/Al_2O_3-h sample was estimated via Fourier shell correlation (FSC) as implemented in the script by Odstrčil *et al.* [4]. The selected region for the FSC is shown in Figure S5 and the obtained FSC with its effective resolution is shown in Figure S6.

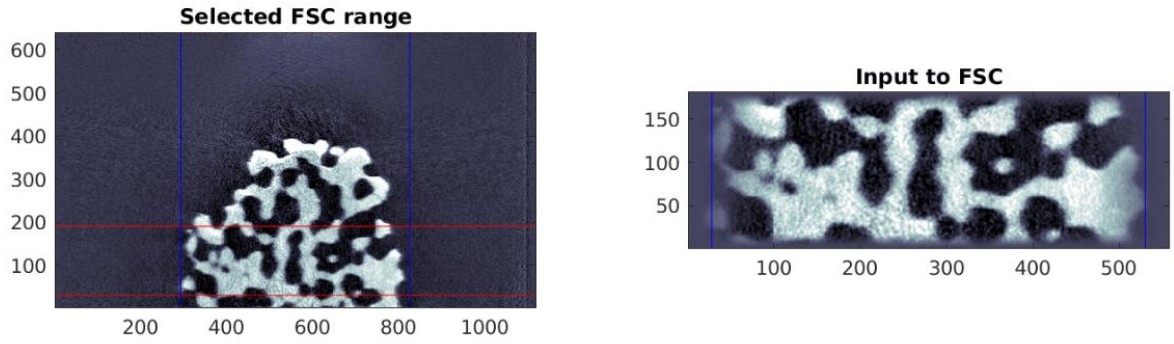

Figure S5 Selected region of the PXCT tomogram of the Ni/Al_2O_3-h sample and resulting input for the FSC analysis

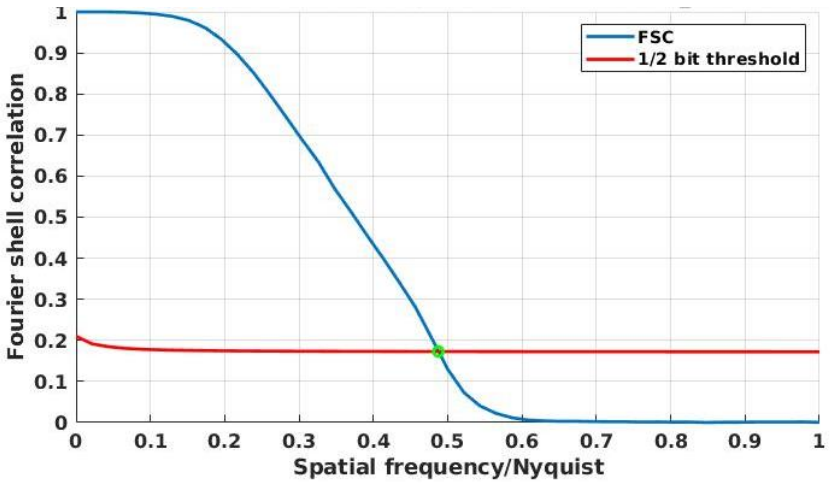

Figure S6 FSC analysis of the $NiAl_2O_3$-h PXCT, the reconstructed pixel size is 38.1 nm and the resolution from the FSC is estimated as 78.3 nm.

2.5. Statistical Values Porosity Analysis

The statistical distribution of the equivalent pore diameter d_{eq} is shown in Figure S7, as obtained from label analysis of the individual labelled pores for the ET and PXCT.

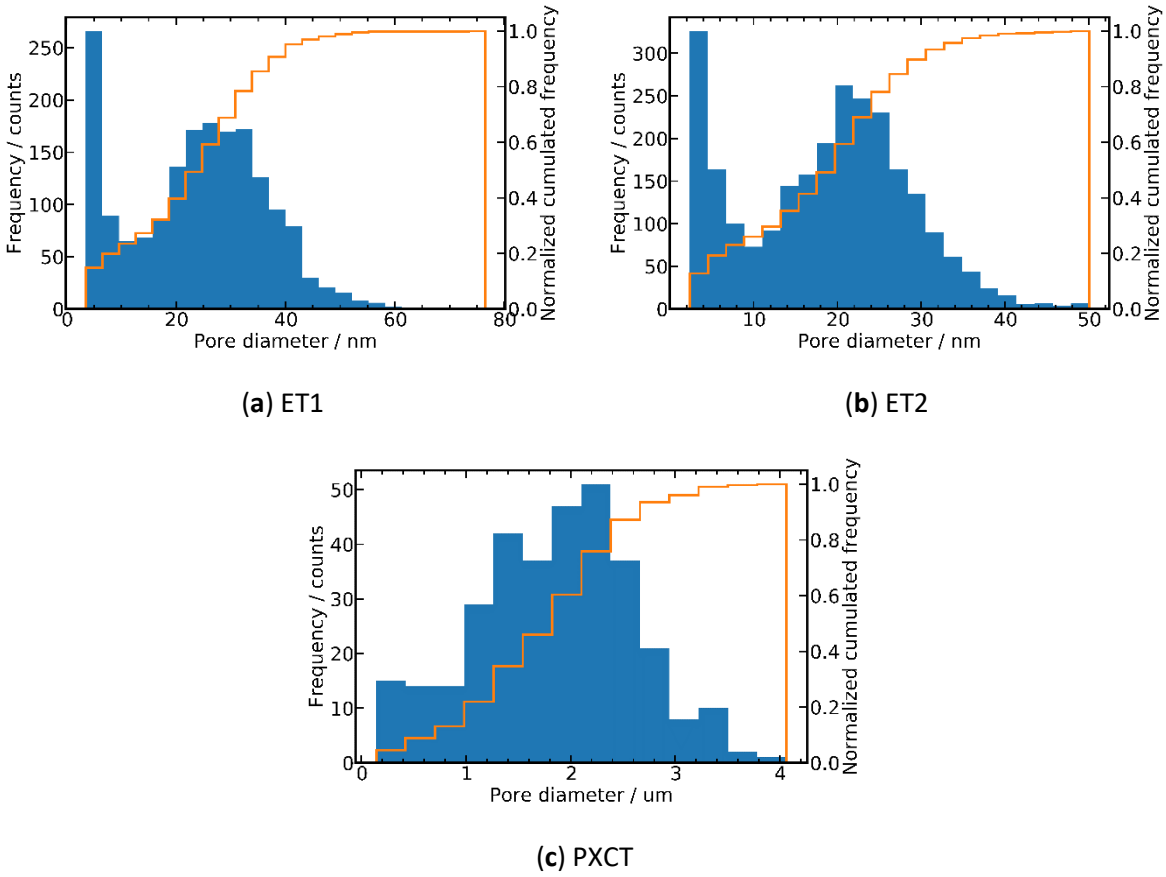

Figure S7 Frequency distribution of different pore diameters obtained from the label analysis of the separated pores from the ET and PXCT experiments of the Ni/Al_2O_3-h catalyst.

3. Catalyst Particle Model

Mass transport and chemical reaction in a steady-state catalyst particle are described by a set of coupled ordinary differential equation for each component $i \in \{CO_2, H_2, CH_4, H_2O\}$ together with their respective boundary conditions:

$$\frac{1}{r^2}\frac{\partial}{\partial r}[r^2 N_i] = \nu_i S \sigma \tag{1}$$

$$N_i = 0 \; at \; r = 0 \tag{2}$$

$$p_i = p_{i,0} \; at \; r = R \tag{3}$$

In these equations r is the radial coordinate in the spherical catalyst particle, R the catalyst particle radius, σ the reaction rate, $N_i$the molar flux, ν_i the stoichiometric coefficient and the p_i partial pressure. As the equations are written as Dirichlet problem, no outer mass transport limitations are considered. Furthermore, the enthalpy balance is neglected, the catalyst particles are assumed as isothermal. As seen from previous simulation studies, both are valid assumptions [5,6]. As the CO_2 methanation reaction is linked to a reduction of number of molecules, pressure gradients may develop in the catalyst particle. In consequence, in addition to the diffusive flux $N_{i,diff}$ also a pressure-driven viscous flux $N_{i,visc}$ is present. The total flux is given by the sum of these fluxes.

$$N_i = N_{i,diff} + N_{i,visc} \tag{4}$$

The diffusive flux of a component i in the porous solid with bimodal pore size distribution is approximately proportional to the product of an effective diffusion coefficient $D_{i,eff}$ and the gradient of its partial pressure:

$$N_{i,diff} = -\frac{D_{i,eff}}{R_{gas}T}\frac{dp_i}{dr} \tag{5}$$

Several models have been proposed for calculating the effective diffusion coefficient in a bimodal porous solid. For example, Wakao and Smith[7] proposed the random pore model. The model is based on the assumption, that diffusion takes place in cylindrical pores in parallel through mesopores with void fraction ε_m, macro-pores with void fraction ε_M and the combination of meso- and macropores in series. According to the model, the effective diffusion coefficient is given by

$$D_{i,eff} = \varepsilon_M^2 D_{i,M} + \frac{\varepsilon_m^2(1+3\varepsilon_M)}{1-\varepsilon_M} D_{i,m} \tag{6}$$

The pore diameter in a porous solid can span several orders of magnitude. In dependence of the mean-free path length of the molecules and the pore diameter, different diffusion mechanisms apply. On the one hand, for very small pores, Knudsen diffusion is the main mechanism of mass transport. On the other hand, for very large pores, molecular diffusion prevails. To interpolate both regimes, the Bosanquet equation is suitable:

$$\frac{1}{D_{i,M/m}} = \frac{1}{D_{i,molec,M/m}} + \frac{1}{D_{i,knud,M/m}} \tag{7}$$

The Knudsen diffusion coefficient is given by

$$D_{i,knud,M/m} = \frac{d_{M/m}}{3}\sqrt{\frac{8R_{gas}T}{\pi M_i}} \tag{8}$$

and the molecular diffusion coefficient in the gas mixture is approximated by the Wilke equation

$$D_{i,molec} = \frac{1 - x_i}{\sum_{j=1,i\neq j}^{N} \frac{x_j}{D_{i,j}}} \tag{9}$$

with binary diffusion coefficient obtained from the Fuller equation [8]:

$$\frac{D_{i,j}}{cm^2/s} = \frac{0.00143\left(\frac{T}{K}\right)^{1.75}\left[\left(\frac{M_i}{g/mol}\right)^{-1} + \left(\frac{M_j}{g/mol}\right)^{-1}\right]^{0.5}}{\frac{p}{bar}\sqrt{2}\left[\Delta_i^{\frac{1}{3}} + \Delta_j^{\frac{1}{3}}\right]} \tag{10}$$

The viscous flux through the porous solid of a component i is given by d'Arcys law as

$$N_{i,visc} = -\frac{x_i B p}{\mu R_{gas} T}\frac{dp}{dr} \tag{11}$$

As the mesopore in the range of 10 nm are considered, the viscous flux will take place mainly in the macropores. Thus, the permeability B is calculated as

$$B = \frac{\varepsilon_M}{\tau_M}\frac{d_M^2}{32} = \varepsilon_M^2\frac{d_M^2}{32} \tag{12}$$

where $\frac{\varepsilon_M}{\tau_M} = \varepsilon_M^2$ according to the random pore model. For cylindrical pores, the specific surface of the catalyst can be calculated in dependence of the void fractions and the pore diameters.

$$S = 4\left(\frac{\varepsilon_m}{d_m} + \frac{\varepsilon_M}{d_M}\right) \tag{13}$$

The reaction kinetics are described by the model of Koschany et al[9]. It was obtained for a $NiAl(O)_x$ catalyst in a temperature range of 180 – 340 °C and pressure range of 1 – 15 bar. As the reaction kinetic model is given in mol/(g_{cat}s), it is converted to mol/(m^2s) by division with the specific surface area of 235 m^2/g_{cat}. As the samples in this study exhibit a lower nickel mass fraction, also lower activities are to be expected. Thus, the reaction rate is further scaled by a constant factor of 0.2.

$$\sigma = 0.2\frac{1}{235\frac{m^2}{g_{cat}}}\frac{k p_{CO2}^{0.5} p_{H2}^{0.5}\left(1 - \frac{p_{CH4}p_{H2O}^2}{K_{eq}p_{CO2}p_{H2}^4}\right)}{\left(1 + K_{OH}\frac{p_{H2O}}{p_{H2}^{0.5}} + K_{H2}p_{H2}^{0.5} + K_{mix}p_{CO2}^{0.5}\right)^2} \tag{14}$$

The catalyst effectiveness factor η is given by the ratio of effective and intrinsic reaction rate

$$\eta = \frac{\sigma_{eff}}{\sigma_{int}} \tag{15}$$

whereas the effective reaction rate of the catalyst particle is given by

$$\sigma_{eff} = \frac{\int_0^R S\sigma r^2 \, dr}{\int_0^R r^2 \, dr} \tag{16}$$

References

[1] Zhou, R.S., Snyder, R.L., *Structures and transformation mechanisms of the η, γ and ϑ transition aluminas*, *Acta Crystallogr. B Struct. Sci. Cryst.* **1991**, *47*, 617-630. 10.1107/S0108768191002719.

[2] St. O'Neill, H.C., Dollase, W.A., Ross II, C.R., *Temperature dependence of the cation distribution in nickel aluminate ($NiAl_2O_4$) spinel: a powder XRD study*, *Phys. Chem. Minerals* **1991**, *18*, 302-319. 10.1007/BF00200188.

[3] Holler, M., Raabe, J., Wepf, R., Shahmoradian, S.H., Diaz, A., Sarafimov, B., Lachat, T., Walther, H., Vitins, M., *OMNY PIN-A versatile sample holder for tomographic measurements at room and cryogenic temperatures*, *Rev. Sci. Instrum.* **2017**, *88*, 113701. 10.1063/1.4996092.

[4] Odstrčil, M., Holler, M., Raabe, J., Guizar-Sicairos, M., *Alignment methods for nanotomography with deep subpixel accuracy*, *Opt. Express* **2019**, *27*, 36637-36652. 10.1364/OE.27.036637.

[5] Schlereth, D., Hinrichsen, O., *A fixed-bed reactor modeling study on the methanation of CO_2*, *Chem. Eng. Res. Des.* **2014**, *92*, 702-712. 10.1016/j.cherd.2013.11.014.

[6] Zimmermann, R.T., Bremer, J., Sundmacher, K., *Optimal catalyst particle design for flexible fixed-bed CO_2 methanation reactors*, *Chem. Eng. J.* **2020**, *387*, 123704. 10.1016/j.cej.2019.123704.

[7] Wakao, N., Smith, J.M., *Diffusion in catalyst pellets*, *Chem. Eng. Sci.* **1962**, *17*, 825-834. 10.1016/0009-2509(62)87015-8.

[8] Verein Deutscher Ingenieure, *VDI heat atlas,* 2. ed; Springer-Verlag Berlin Heidelberg, Berlin, 2010.

[9] Koschany, F., Schlereth, D., Hinrichsen, O., *On the kinetics of the methanation of carbon dioxide on coprecipitated $NiAl(O)_x$*, *Appl. Catal. B* **2016**, *181*, 504-516. 10.1016/j.apcatb.2015.07.026.